Multiscale iterative voting for differential analysis of stress response for 2D and 3D cell culture models

J. HAN, H. CHANG, Q. YANG, G. FONTENAY, T. GROESSER, M. HELEN BARCELLOS-HOFF & B. PARVIN
Lawrence Berkeley National Laboratory, Berkeley, CA, U.S.A.

Summary

Three-dimensional (2D) cell culture models have emerged as the basis for improved cell systems biology. However, there is a gap in robust computational techniques for segmentation of these model systems that are imaged through confocal or deconvolution microscopy. The main issues are the volume of data, overlapping subcellular compartments and variation in scale or size of subcompartments of interest, which lead to ambiguities for quantitative analysis on a cell-by-cell basis. We address these ambiguities through a series of geometric operations that constrain the problem through iterative voting and decomposition strategies. The main contributions of this paper are to (i) extend the previously developed 2D radial voting to an efficient 3D implementation, (ii) demonstrate application of iterative radial voting at multiple subcellular and molecular scales, and (iii) investigate application of the proposed technology to two endpoints between 2D and 3D cell culture models. These endpoints correspond to kinetics of DNA damage repair as measured by phosphorylation of γH2AX, and the loss of the membrane-bound E-cadherin protein as a result of ionizing radiation.

Preliminary results indicate little difference in the kinetics of the DNA damage protein between 2D and 3D cell culture models; however, differences between membrane-bound E-cadherin are more pronounced.

Introduction

Current models of high-content screening are based on 2D cell culture models that are grown either on plastic or on glass. Although such a model system may be appropriate as an initial step towards discovery or for certain aspects of biological studies, the knowledge may not be readily extensible

Correspondence to: Bahram Parvin, Lawrence Berkeley National Laboratory, 1 Cyclotron Road Mail Stop 977R250, Berkeley, CA 94720, U.S.A. Tel: +1 510 486 6203; fax: +1 510 486 5586; e-mail: b_parvin@lbl.gov

to *in vivo* models. By contrast, animal studies are expensive and time-consuming, and as a result cannot scale for large studies that are necessary to build a space–time continuum of responses in the presence of biological heterogeneity. An intermediate step is 3D cell culture model systems, which have been demonstrated to have some of the functionalities of the *in vivo* models (Weaver *et al.*, 1996). However, such a model system introduces significant computational challenges: (i) imaging is in 3D and not in the projection space; (ii) subcellular compartments often overlap, and as a result, delineation of each compartment becomes more challenging computationally and (iii) variations in scale impose a more complex segmentation problem at the object level. These complexities are illustrated in a series of serial sections of Fig. 1, where the 3D cell culture model, known as a mammosphere, is composed of epithelial cells, which are polarized and form a hollow sphere. This polarized architecture is necessary for its functional behaviour such as production of milk in culture. It is important to quantify morphology and localization on a cell-by-cell basis in these assays. Therefore, segmentation of subcellular compartments is essential for detailed quantitative analysis.

Our basic segmentation strategy is to leverage saliency, which is a well-known concept in the computer vision. In the case of data, shown in Fig. 1, saliency corresponds to approximate radial symmetry as all nuclei are blob-like and compact. Radial symmetry is a special class of symmetry, which can be visualized at multiple scales of nuclear morphology and nuclear foci (e.g. PML bodies Stuurman *et al.*, 1990). Therefore, robust and efficient detection of inexact radial symmetries facilitates the semantic representation of images for summarization and interpretation. Yet, the notion of radial symmetry is used in a weak sense because the basic geometry can deviate in scale, aspect ratio and convexity.

In this paper, we present a geometric-based method for delineating 3D cell culture models for structural as well as functional analysis. The novelty of the proposed method is in specific geometric steps, shown in Fig. 2, which are designed
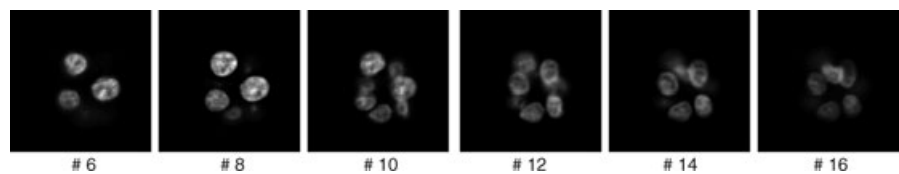
Fig. 1. Slices of a 3D mammosphere along the Z-direction indicate that in some planes subcellular regions overlap; however, a weak convexity constraint and radial symmetry can provide the necessary bound for delineating individual compartments. The resolution along the *XY*-axis is eight times of the Z-axis.

to bound the solution through seeding and subsequent partitioning. At the coarse scale, estimation of the nuclear centroid in a mammoshpere enables partitioning of touching nuclei, which is performed by finding planes that best separate touching cells. The actual methodology is based on the Radon transform. The Radon transform is the integral transform in an N-dimensional space, whose value at each point is the integral over the $(N - 1)$-dimensional manifold orthogonal to the vector represented by that point (Deans, 1983). At the fine scale, localization of punctate signals (e.g. small macromolecular structures) within each nucleus enables an accurate representation of each event. The small regions of the target protein (e.g. $1-2\,\mu$m for the DNA repair protein) are first detected through radial voting and then segmented by representing the immediate local region as a mixture of two Gaussians whose parameters are estimated through the
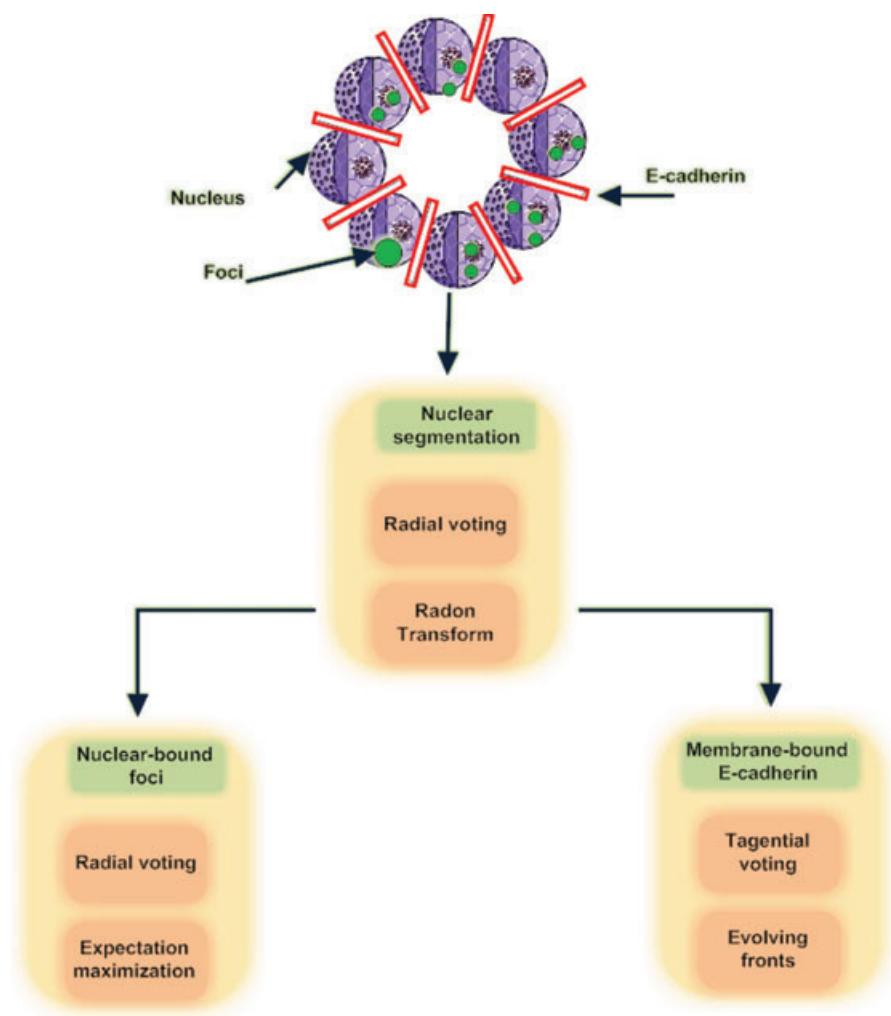

Fig. 2. Steps in quantitative analysis of mammosphere architecture and different endpoints. The first step is to nuclear segmentation, which provides context for either nuclear-bound foci analysis or cell-surface bound E-cadherin (painted as red) analysis. It is important to note that radial voting is applied at two scales to detect nuclei as well small macromolecule objects such as foci (painted as green).

expectation–maximization algorithm. At both scales, seeding (e.g. approximating centres of mass) is based on iterative spatial voting, and is implemented through the refinement of specifically tuned voting kernels (Parvin *et al.*, 2007), which is extended to 3D in this paper.

Spatial voting has been studied for at least four decades. A classic example of spatial voting is the Hough transform for detecting parametric objects (e.g. circle, ellipse, line). The Hough transform has also been extended into the generalized Hough transform (Duda & Hart, 1972), which is compute and memory intensive. Our approach defines a series of kernels that can vote iteratively along the radial or tangential edge directions. These kernels are designed to accentuate a specific saliency (e.g. centre of mass, linear structures). Voting along the radial direction leads to estimation of the centre of mass, whereas voting along the tangential direction enforces continuity. However, as it is in the case with Hough for detecting circles, voting can be very noisy. However, we have shown that through iterative voting (Parvin *et al.*, 2007), noisy inference of spatial clusters can be reduced and eliminated. Therefore, by iterative refinement of kernel domain and orientation, spatial clustering is significantly improved.

Our contributions are two folds. First, we will present an efficient implementation of 3D voting for seed detection and apply to real biological endpoints for segmentation and quantitative analysis. Here, endpoint refers to an observed or measured outcome to indicate or reflect the effect of the experiment. Secondly, we will present two endpoints that are differentially expressed between 2D and 3D cell culture models. One endpoint is nuclear-bound, whereas the second one is cell-membrane-bound providing an excellent contrast for differential analysis. The details of membrane-bound endpoint has been extensively described in our previous papers (Chang *et al.*, 2007; Han *et al.*, 2010), and is primarily used as a point of discussion in this paper.

The organization of this paper is as follows. Section 2 provides a brief review of the previous research. Section 3 describes geometric steps (e.g. voting, coarse tessellation and Radon transform) and the detailed implementation. Section 4 discusses the experimental results. Section 5 concludes the paper.

Previous research

A critical component of image analysis is segmentation, which provides context for multidimensional profiling (Carpenter *et al.*, 2006). The current practice is to label the nuclear region with a DNA stain to provide context for detailed morphological analysis and further protein localization. Although most of the current computational models have been developed for 2D cell culture models, they should be extensible to 3D models as well. The key concepts have been watershed (Chawala *et al.*, 2004), geometric method (Raman *et al.*, 2007; Wen *et al.*, 2009) and active surface models for segmentation of nuclear regions

(Sarti *et al.*, 2000; Padfield *et al.*, 2009; Srinivasa *et al.*, 2009). A recent comparison of traditional nuclear segmentation method has been addressed in (Coelho *et al.*, 2009), where the main issue has been to delineate touching nuclei and to enable measurements on a cell-by-cell basis. Several flavours of nuclear segmentation are summarized later.

In Byun *et al.* (2006), detection of nuclear regions is modelled through Laplacian of Gaussian (LoG). The response from the LoG filter is then analysed for peak detection corresponding to the centre of mass for each nucleus. The method is noniterative, incorporates a fixed filter size, and is appropriate when nuclear morphology is relatively homogeneous. This is essentially a detection technique, however, it does provide some constraints to bound the segmentation problem. In Lin *et al.* (2003), segmentation and classification are tightly coupled for a model-based framework. The process is initiated from a watershed-based method, which partitions the image and potentially fragments each nucleus. Through an efficient hierarchical strategy, two or more fragments are merged together to form a candidate. Each candidate is then scored to guide the merging process. The final blob is also classified against one of the models to reveal the nuclear type. However, the segmentation results are sensitive to initial conditions for the generation of 'merge tree'. In Li *et al.* (2007), a method based on regularization of the gradient vector flow is proposed. This method is roughly an extension of the regularized centroid transform (Yang & Parvin, 2003) to 3D data. The basic idea is to apply the gradient flow tracking algorithm to label each pixel with a converged sink position that corresponds to cell centroid. The method is iterative, compute intensive and has been applied to low-resolution fluorescence images. The main limitation of this method are that (i) multiple sinks may be detected for elongated nuclei and (ii) it assumes that the nuclear intensity is homogeneous and does not contain obvious inner structures. In Nath *et al.* (2006), an efficient implementation of level set method (Chan & Vese, 2001) is proposed by reducing complexities associated with the original multiphase implementation (Vese & Chan, 2002). They leverage the four-colour property of the spatial organization of different objects to reduce the number of evolving fronts. The net result is an efficient implementation, by reducing the number of coupling terms, which has been applied to tracking cells in wound-healing assays. These assays are imaged through phase contrast microscopy, however, initialization can be a potential problem for fixed cells with overlapping compartments. Finally, a number of researchers have focused on phenotypic subtyping and modelling (Jackson *et al.*, 2009; Yin *et al.*, 2009; Coelho *et al.*, 2010).

To our knowledge, the literature on segmentation of mammosphere structures is limited to a system, where segmentation is performed in 2D followed by merging segmented results in a 3D stack (Knowles *et al.*, 2006). This particular assay produces nuclear regions that tend to be separable in 2D (e.g. little overlap) while maintaining a similar

scale in nuclear size. Heterogeneity in these assays originates from the cell line and specific treatments that they have undergone. Iterative voting tends to be more tolerant to scale. As a result, it is an excellent low level modules for identifying pertinent seeds.

Approach

In this section, we will address the details for segmentation of (i) nuclei and (ii) nuclear-bound macromolecules, where both tasks utilize the same computational strategy. Details of membrane-bound signal are only presented at high level and as a point of discussion in the next section.

Initially, the 3D stack of data is normalized for an isotropic representation so that X, Y and Z have similar physical dimensions. In the nuclear channel, seeds are detected using radial voting and the image is adaptively thresholded using the Otsu's method (Otsu, 1979) in parallel. Each clump of cells are then decomposed at two levels using Radon transform and Voronoi tessellation. Segmentation of nuclear regions provides context for delineation of membrane-bound macromolecules (e.g. PML bodies). Accordingly, seeds are detected with a different parameter settings and each foci is segmented by modelling foreground and background as a mixture of two Gaussians.

Nuclear seed estimation with iterative radial voting

The basic concept is that important information are visualized along the edges, and by projecting the gradient information with specialized kernels, seeds corresponding to the centre of mass can be detected. This is an iterative method, and the kernel topography is smooth and becomes more focused and dense at each iteration. The method extends our previous effort, which restrict voting to a 2D plane (Parvin *et al.*, 2007). Let $I(\mathbf{x})$ be the original image, where the domain points $\mathbf{x} = (x, y, z)$ are 3D image coordinates. Let $\mathbf{a}(\mathbf{x})$ be the voting direction at each 3D image point, where $\mathbf{a}(\mathbf{x})$ is a unit vector that varies with the image location. Let $\{r_{\min}, r_{\max}\}$ be the radial range and Δ be the angular range. Let $V(\mathbf{x}; r_{\min}, r_{\max}, \Delta)$ be the 3D vote image, dependent on the radial and angular ranges and have the same dimensions as the original 3D image. Let $v(\mathbf{x}; r_{\min}, r_{\max}, \Delta)$ be the local voting volume, defined at each image point $\mathbf{x}$ and dependent on the radial and

angular ranges, defined by

$$v(\mathbf{x}; r_{\min}, r_{\max}, \Delta) := \{\mathbf{x} \pm \mathbf{p} | r_{\min} \leq \|\mathbf{p}\| \leq r_{\max},$$
$$\text{and } 0 \leq \angle\{\mathbf{p}, \mathbf{a}(\mathbf{x})\} \leq \Delta\}. \quad (1)$$

Finally, let $K(\mathbf{x}; \sigma, \mathbf{a}, v)$ be a 3D Gaussian kernel (e.g. $g(x, y, z) = (1/\sqrt{2\pi}\sigma)e^{-(x^2+y^2+z^2)/2\sigma^2}$ with variance σ^2, masked by the local voting volume $v(\mathbf{x}; r_{\min}, r_{\max}, \Delta)$), and oriented in the voting direction $\mathbf{a}(\mathbf{x})$. Figure 3 shows a subset of voting kernels that vary in topography, scale and orientation. For simplicity, only the 2D intersection along the axis of the cone kernel is shown in this figure.

The iterative voting algorithm is outlined later.

Iterative Voting

(1) *Initialize the parameters:* Initialize $r_{\min}, r_{\max}, \Delta_{\max}$ and a sequence $\Delta_{\max} = \Delta_N > \Delta_{N-1} > \cdots > \Delta_0 = 0$, where N is the number of iterations. Set $n = N$ and the vote image $V(\mathbf{x}; r_{\min}, r_{\max}, \Delta_{N+1}) = 0$. Also fix a low gradient threshold, Γ_g, and a kernel variance, σ, depending on the expected scale of salient features.

(2) *Initialize the saliency feature image:* Define the feature image $F(\mathbf{x})$ to be the local external force at each pixel of the original image. The external force is often set to the gradient magnitude or maximum curvature, depending upon the type of saliency and the presence of local feature boundaries.

(3) *Initialize the voting direction and magnitude:* Compute the image gradient, $\nabla I(\mathbf{x})$, and its magnitude, $\|\nabla I(\mathbf{x})\|$. Define a pixel subset $S := \{(\mathbf{x})| \|\nabla I(\mathbf{x})\| > \Gamma_g\}$. For each grid point $(\mathbf{x}) \in S$, define the voting direction to be

$$\mathbf{a}(\mathbf{x}) := -\frac{\nabla I(\mathbf{x})}{\|\nabla I(\mathbf{x})\|}.$$

(4) *Compute the votes:* For each pixel $\mathbf{x} \in S$, update the vote image as follows:

$$V(\mathbf{x}; r_{\min}, r_{\max}, \Delta_n) := V(\mathbf{x}; r_{\min}, r_{\max}, \Delta_{n+1})$$
$$+ \sum_{\mathbf{u} \in v(\mathbf{x}; r_{\min}, r_{\max}, \Delta_n)} F(\mathbf{x} + \mathbf{u}) K(\mathbf{u}; \sigma, \mathbf{a}, v).$$

(5) *Update the voting direction:* For each grid point $\mathbf{x} \in S$, revise the voting direction. Let $\mathbf{u}^* = \arg\max_{\mathbf{u} \in v(\mathbf{x}; r_{\min}, r_{\max}, \Delta_n)} V(\mathbf{u}; r_{\min}, r_{\max}, \Delta_n)$. Let $\mathbf{d_x} = \mathbf{u}^* - \mathbf{x}$, and $\mathbf{a}(\mathbf{x}) = \frac{\mathbf{d_x}}{\|\mathbf{d_x}\|}$.

(6) *Refine the angular range:* Let $n := n - 1$, and repeat steps 4–6 until $n = 0$.
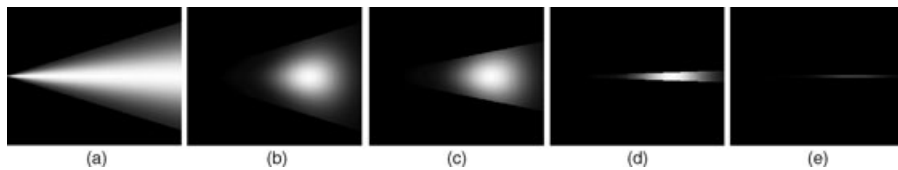

Fig. 3. Kernel topography in 2D: (a–e) Evolving kernel for the detection of radial symmetry (shown at a fixed orientation) has a trapezoidal active area with Gaussian distribution along both the radial and tangent axes.

(7) *Determine the points of saliency:* Define the centres of mass or completed boundaries by thresholding the vote image:

$$C = \{\mathbf{x} | V(\mathbf{x}; r_{\min}, r_{\max}, \Delta_0) > \Gamma_v\}.$$

The voting algorithm contains a number of parameters that are defined as follows:

- *Voting volume:* For radial voting, the algorithm can be tuned to look exclusively for dark or bright objects, or both, by selecting the signs in Eq. (1), which dictate whether the kernels are oriented in the direction of positive or of negative gradient. For bright objects $v(\mathbf{x}; r_{\min}, r_{\max}, \Delta)$ is set to

$$v^+(\mathbf{x}; r_{\min}, r_{\max}, \Delta) := \{\mathbf{x} + \mathbf{p} | r_{\min} \leq \|\mathbf{p}\| \leq r_{\max},$$
$$\text{and } 0 \leq \angle\{\mathbf{p}, \mathbf{a}(\mathbf{x})\} \leq \Delta\}.$$

For dark objects, $v(\mathbf{x}; r_{\min}, r_{\max}, \Delta)$ is set to

$$v^-(\mathbf{x}; r_{\min}, r_{\max}, \Delta) := \{\mathbf{x} - \mathbf{p} | r_{\min} \leq \|\mathbf{p}\| \leq r_{\max},$$
$$\text{and } 0 \leq \angle\{\mathbf{p}, \mathbf{a}(\mathbf{x})\} \leq \Delta\}.$$

- *Voting magnitudes:* The voting profile contributed by each pixel is a function of its strength (e.g. gradient magnitude). Weak features can be thresholded with a small value, Γ_g, to improve computational efficiency; however, this is not a necessary step. It is the edge magnitude and organization of edges that contribute to the voting landscape, thus suppressing random noise even further.

- *Radial and angular ranges:* The bounds $r_{\min}$ and $r_{\max}$ on the radial range, and the maximum angular range $\Delta_{\max}$ are preselected given the shapes of the objects to be detected. For example, to detect circles, we can set $r_{\min} = r_{\max}$ and $\Delta_{\max} = 0$, and to detect ellipsoids of the form $\frac{x^2}{a^2} + \frac{y^2}{b^2} + \frac{z^2}{c^2} = 1$, we set $r_{\min} = \min(a, b, c)$, $r_{\max} = \max(a, b, c)$ and $\Delta_{\max} = \max\{\arcsin\frac{|a^2-b^2|}{a^2+b^2}, \arcsin\frac{|a^2-c^2|}{a^2+c^2}, \arcsin\frac{|b^2-c^2|}{b^2+c^2}\}$, which is the maximum angle between the radial and the gradient (normal) vectors of the ellipsoids. Although these are ideal cases, tolerances are added for real-world images.

- *Step-size in the evolution of kernel shape:* An important value in the protocol is the step-size with which the voting volume is iteratively reduced. If the step-size is too large, then the centres of mass or boundaries will be fragmented, and, if it is too small, then the computational cost will rise. The monotonically decreasing sequence, $\Delta_{\max} = \Delta_N > \Delta_{N-1} > \cdots > \Delta_0 = 0$, controls the convergence rate of the algorithm. Each time the voting direction is updated, the angular range is decreased to shrink the voting volume. In our system, the interval $[0, \Delta_{\max}]$ is equally partitioned, and the maximum value is set interactively. For an object demonstrating simple circular geometry, a few iterations (e.g. $N = 4$) is adequate. A higher value is necessary for noisy images with overlapping objects.

- *Threshold of output image:* The final vote image is always ranked. In some cases, a threshold Γ_v may be set to select the most prominent set of hypotheses.

To analyse the computational complexity of the iterative voting, let us examine the voting volume defined by Eq. (1). The cost of generating such a voting volume is very high. To solve this problem, a voting direction can be quantized into angular bins, and a template voting area may be generated and stored for each angular bin. Compared to the voting operation, the cost of precomputing and searching these templates can be ignored. The computational complexity of performing a single voting operation at iteration n is $O(K(r_{\max}^2 - r_{\min}^2)\Delta_n)$, where K is the number of pixels in the original image. If we select the sequence of angular ranges to be $\Delta_n = \Delta_{\max}n/N$, where N is the number of iterations, then the total complexity of the voting operations is $\sum_{n=0}^{N} K(r_{\max}^2 - r_{\min}^2)\Delta_{\max}n/N = O(KN)\Delta_{\max}(r_{\max}^2 - r_{\min}^2)$. Essentially, the complexity is determined by the image size and the predetermined radial and angular ranges. If the objects are known to be nearly round, then $\Delta_{\max}$ and $r_{\max}^2 - r_{\min}^2$ can be set to be quite small, and $O(KN)\Delta_{\max}(r_{\max}^2 - r_{\min}^2)$ may be reduced to as low as $O(KN)$.

To illustrate the behaviour of iterative voting, Fig. 4 shows intermediate steps that lead towards final results for a 3D mammosphere. The voting landscape corresponds to the spatial clustering that is initially diffuse and is subsequently refined and focused into distinct regions. Notice that the proposed voting algorithm successfully detected the seeds for 3D overlapping objects with various size. An example of the 3D voting result is shown in Fig. 5, where each nucleus in a mammosphere has been detected.

Iterative voting shares a common thread with optimization problems in computer vision, which rely on establishing proper geometric constraints and then regularizing the solution. In this case, geometric constraints are expressed in the *shape* of the voting kernel and the regularization is embedded in the smoothness of kernel. The iterative process leads the solution into its local minima by searching for the maximum response in a local neighbourhood. The iterative nature of scalar voting reduces the possibility of generating multiple seeds within the same region, provides a tight geometric constraint on the shape of each subcompartment, and improves the overall efficiency of the computational pipeline.

Partitioning of a mammosphere from seeded nuclei

The process is initiated by a coarse segmentation of nuclei with a 3D Voronoi tessellation. First, initial tessellation facilitates identification of a local neighbourhood where each nuclear region is contained within its own space. As a result, this provides the possibility of partitioning touching nuclei through the Radon transform, which has to be performed on a neighbourhood which contains one pair of touching nuclei only. For example, the Radon transform will fail in partitioning two touching nuclei when the local neighbourhood contains the third nucleus, as shown in Fig. 6 from real data. Secondly,
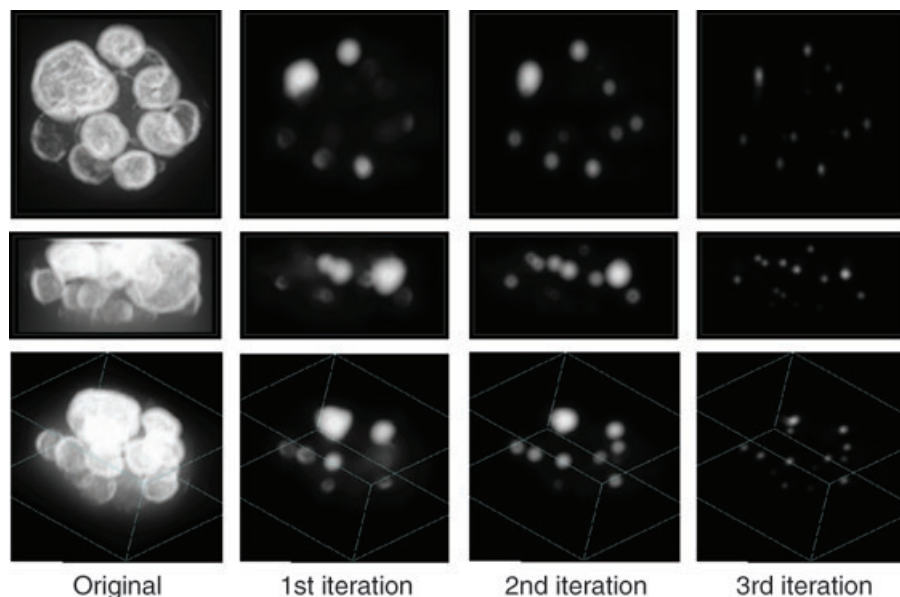
Fig. 4. Detection of radial symmetries for a real 3D image with multiple overlapping objects where voting landscapes are shown from different views. First row – top view; second row – side view; third row – 3D view.
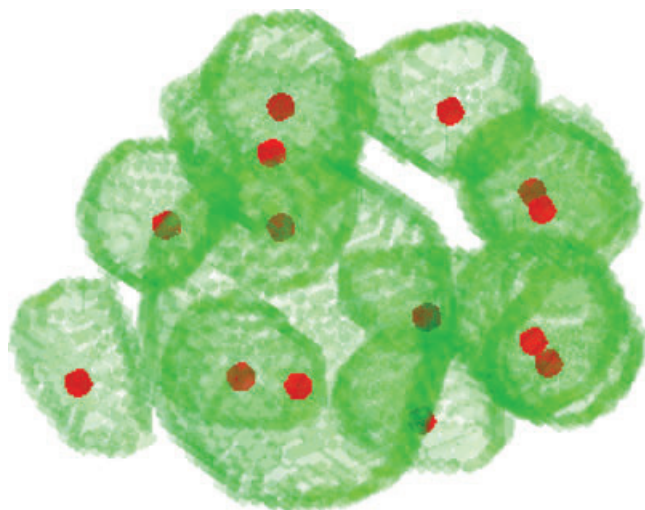

Fig. 5. Voted results projected on the multicellular system of Fig. 4.

initial tessellation improves computational performance for each mammosphere prior to Radon transform. This feature has to do with the fact that not all adjacent nuclei are connected and that there is a clear empty space between them. Under this condition, there is no need to refine the segmentation further.

The details of Radon transform are as follows; however, for simplicity the 2D version is described first. The Radon transform represents an image as a collection of projections in a function domain $f(x, y)$ along various lines defined by the shortest distance ρ from the origin and the angle of inclination

θ with the y axis

$$R(\rho, \theta) = \int \int f(x, y)\delta(\rho - x \cos \theta - y \sin \theta)\mathrm{d}x\mathrm{d}y.$$

(2)

Properties of the Radon transform enable segmentation of nearby touching objects. For example, two adjacent objects, represented by circles in Fig. 7(a), and their corresponding Radon transform shown in Fig. 7(b), have a local minimum that is located at $\rho = 17$ and $\theta = 135°$. This local minimum corresponds to the integration over the line that separates the two objects with the smallest cross section.

Similarly, the 3D Radon transform represents a 3D volume as a collection of projections in a function domain $f(x, y, z)$ along various planes defined by the shortest distance ρ from the origin, the angle of azimuth ϕ around the z axis and the angle of elevation θ around the y axis

$$R(\rho, \phi, \theta) = \int \int \int f(x, y, z)\delta(\rho - x \cos \phi \cos \theta - y \sin \phi \cos \theta - z \sin \theta)\mathrm{d}x\mathrm{d}y\mathrm{d}z.$$

The Radon transform is a separable transform and its implementation is shown in Fig. 8. A fast method for computing 3D radon transform via a direct Fourier method can be found in (Lanzavecchia & Luigi Bellon, 1998). Given a local cube containing two nearby adjacent cells, each of which is bounded by a seed, the optimal plane separating these two cells should be located between the two seeds and have the smallest cross section. The local minimum in the 3D Radon transform corresponds to the integration over the optimal plane in the local cube. The final segmentation of
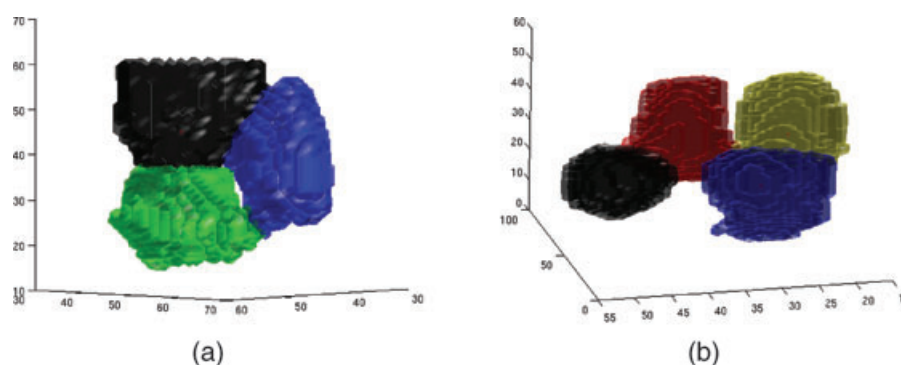
Fig. 6. A segmented visualization of the nuclear configuration where tessellation (tessellation is not shown) enforces locality: (a) the blue nucleus resides at the fold between the green and black nuclei (and without an initial tessellation subsequent Radon transform refinement will fail) and (b) empty spaces between black and blue nuclei eliminate the need for Radon transform refinement.

a mammosphere for the stack shown in Fig. 4 is shown in Fig. 9.

Fig. 8. The Radon transform is separable, and the 3D Radon transform can be decomposed into a series of 2D Radon transforms.

Foci seed estimation with iterative voting

Nuclear segmentation can provide context for quantitative assessment of protein signal, which can be punctate and small. An example of such small signals is the DNA repair protein shown in Fig. 10 shows a slice from a mammosphere, indicating nuclear region and corresponding foci that are formed by phosphorylation of histone γH2AX following ionizing radiation. Following nuclear segmentation, a foci image is created through maximum project of foci channel within each nucleus. As a result, detection of foci is performed in 2D because accidental alignment of two foci in a Z-stack is very rare.

At this scale, foci can also be detected by radial voting with smaller parameter settings. This kind of functionality is often referred to as an interest point operator, and there
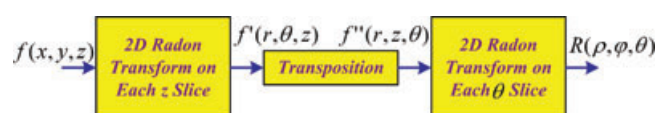
is a large literature on this topic, but iterative voting is robust and can distinguish overlapping events. However, segmentation of these punctate events can be complicated as a result of variation in (1) background intensity, (2) foreground intensity, (3) sample preparation, (4) instrument configuration and (5) nearby signals. Our approach is based on (1) establishing a local neighbourhood, bounded by the maximum size of foci, and (2) modelling the local intensity distribution as a mixture of two Gaussian, whose latent variables are estimated using the expectation–maximization method (Bilmes, 1997).
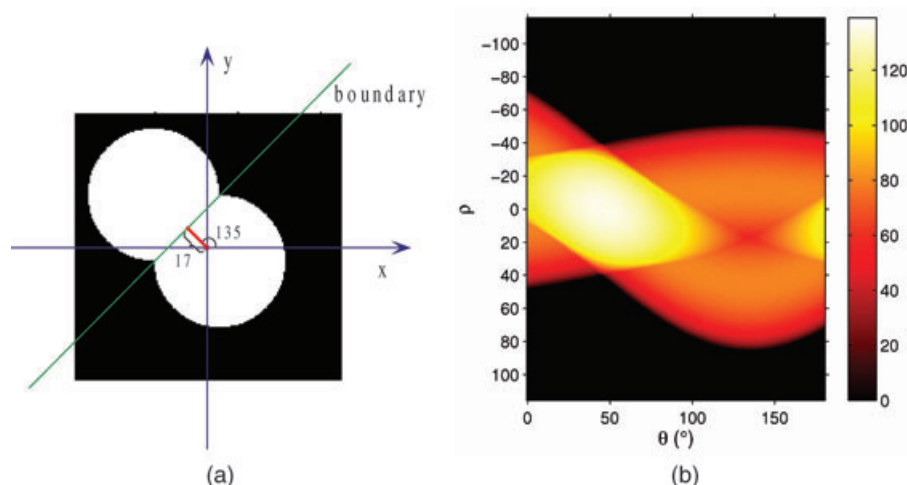

Fig. 7. An example of 2D object segmentation using the Radon transform: (a) synthetic object composed of two circles and (b) corresponding Radon transform with local minimum at $\rho = 17$ and $\theta = 135°$.
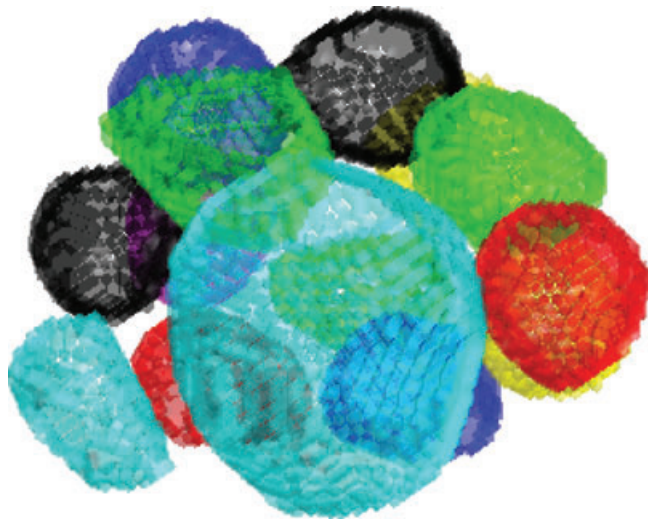
Fig. 9. Final segmentation of a mammosphere for the stack shown in Fig. 4.

Quantification of the Membrane-bound E-cadherin

In this section, we briefly summarize a computational method for quantifying membrane-bound macromolecules such as E-cadherin, where the details have already been published (Chang *et al.*, 2007; Han *et al.*, 2010). The significance of this endpoint is that E-cadherin regulates cell–cell interactions and physical properties of tissues, and loss E-cadherin has been associated with (i) increased motility, (ii) cancer progression and metastasis and (iii) increased resistance to cell death (Cavallaro & Christofori, 2004). The main rationale is a case study for examining membrane- and nuclear-bound endpoints, in 2D and 3D cell culture models, as a result of ionizing radiation. Our published approach to delineate and quantify E-cadherin signal has three steps: (i) nuclei are segmented to provide context and initialization for subsequent steps; (ii) membrane-bound E-cadherin is enhanced and regularized through iterative tangential voting (Chang *et al.*, 2007) and (iii) evolving fronts, originating from each nucleus, are attracted to the regularized membrane signal (Chang & Parvin, 2010; Han *et al.*, 2010). An example for the effect of tangential voting for a 3D cell culture model is shown in Fig. 11. Tangential voting fills gaps and regularizes the signal.

Experimental results

The primary contribution of this paper is in the development of the 3D radial voting and developing a system for delineating individual nucleus in a mammosphere. The secondary contribution is its application to real biological problems. First, we present validation of the computational pipeline. Secondly, we apply the method to several data sets.

Validation of seed detection with synthetic data

A synthetic data set has been generated to evaluate the proposed approach. This data set contains 30 image stacks with 350 pixels in X, Y and Z dimensions, respectively. Each
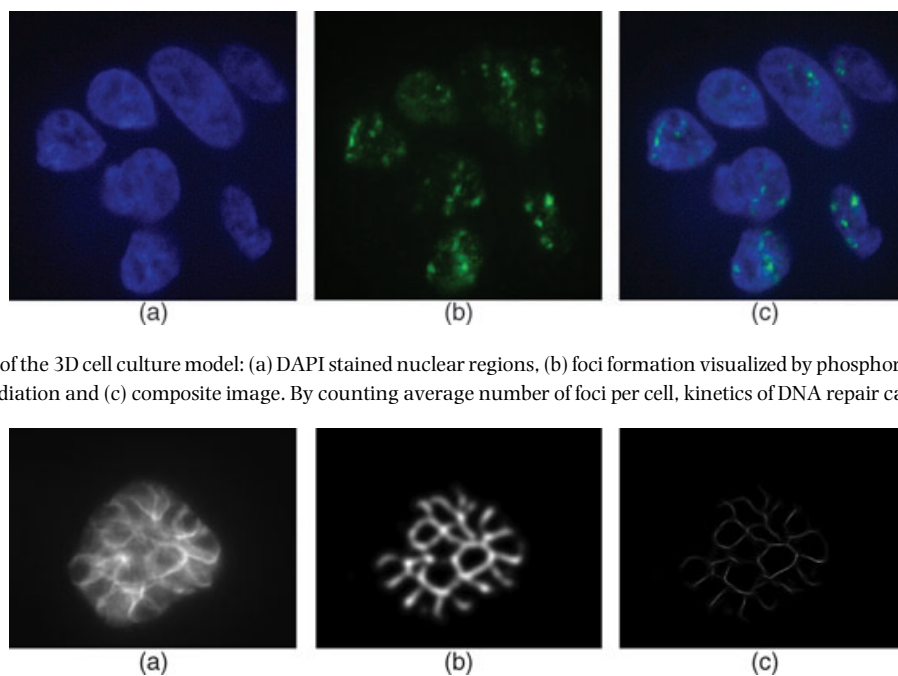

Fig. 10. A cross section of the 3D cell culture model: (a) DAPI stained nuclear regions, (b) foci formation visualized by phosphorylation of histone γH2AX as a result of ionizing radiation and (c) composite image. By counting average number of foci per cell, kinetics of DNA repair can be quantified.

Fig. 11. Localization of E-cadherin in a multicellular system: (a) a slice of the original image of the mammosphere (3D cell culture model), (b) initial voting landscape and (c) voted results corresponding to the membrane proteins along the points of maximum negative curvature.

Table 1. Nuclear under-detection error (percentage of undetected nuclei) on synthetic data at different noise levels (σ).

3-10 r_{max}	Δ_{max}	Noise level (σ)							
		0	100	200	300	400	500	600	700
50	20	0	0	0	0	0.19%	0	0.19%	0
50	25	0.19%	0	0	0	0	0	0	0
50	30	0	0	0	0	0	0	0	0
60	20	0	0	0	0	0	0	0	0
60	25	0	0.19%	0	0	0	0	0	0
60	30	0	0	0	0	0	0	0	0
70	20	0.74%	0.56%	1.30%	0.74%	0	0	0	0
70	25	1.85%	0.74%	0.74%	0.37%	0	0	0	0
70	30	0.74%	0.93%	0.74%	0.56%	0	0	0	0
80	20	0.74%	0.74%	0.93%	0.93%	0.19%	0	0.37%	0
80	25	1.67%	1.67%	2.22%	1.48%	0	0	0	0
80	30	1.48%	0.93%	1.30%	0.74%	0	0	0	0

image stack contains 18 cells whose centres are located on the surface of a sphere with a radius of 100 pixels. This sphere corresponds to an idealized and normal representation of mammosphere. The centroid of each cell is set at 100, (0,0), (−100,0,0), (0,100,0), (0,−100,0), (0,0,100), (0,0, −100), (71,71,0), (−71,71,0), (71,−71,0), (−71,−71,0), (71,0,71), (−71,0,71), (71,0,−71), (−71,0,−71), (0,71,71), (0,−71,71), (0,71,−71), (0,−71,−71), however, these centroids are uniformly perturbed, with ±5 pixels, along each axis. The principal axes, orientation and intensity of each cell are randomly generated from to create varying amounts of overlap between neighbouring cells and diversity in staining (or cell cycle state). More specifically, the principal axes are generated from a uniform distribution between 60 and 100 pixels, foreground and background intensities are set at 1200 and 600 and intensity is corrupted by varying amount of Gaussian noise $\mathcal{N}(0, \sigma)$. The iterative radial voting algorithm is then applied to estimate the centroid of each nucleus in the 3D image stack. A subset of the voting parameters, such as $r_{min} = 1$ and $\Gamma_g = 50$, have minimal effect on the final outcome, and, therefore, are fixed in this experiment. We evaluate the nuclear detection performance by varying r_{max}, Δ_{max} and added noise (σ). The performance of the nuclear seed detection is evaluated based on two errors: percentage of missing seeds and percentage of extra seeds. Table 1 shows the percentage of missing seeds on synthetic data at different levels of added noise, which indicates low error rate, insensitivity to parameters r_{max} and Δ_{max}, and the noise level σ. Table 2 shows the result of the second experiment on quantifying detection of extraneous seeds on the same data set. Again, we

Table 2. Nuclear over-detection error (percentage of multidetected nuclei) on synthetic data at different noise levels (σ).

3-10 r_{max}	Δ_{max}	Noise level σ							
		0	100	200	300	400	500	600	700
50	20	0.74%	0.56%	0.56%	0.37%	0.19%	0.37%	0.93%	2.78%
50	25	0.56%	0.56%	0.56%	0.37%	0.19%	1.30%	2.59%	7.96%
50	30	0.56%	0.56%	0.37%	0.37%	0.74%	3.15%	4.63%	7.78%
60	20	0	0	0	0	0	0	0	0.19%
60	25	0	0	0	0	0	0	0	0.37%
60	30	0	0	0	0	0	0.19%	0.56%	1.11%
70	20	0	0	0	0	0	0	0	0
70	25	0	0	0	0	0	0	0	0.19%
70	30	0	0	0	0	0	0	0	2.04%
80	20	0	0	0	0	0	0	0.19%	0.37%
80	25	0	0	0	0	0	0	0	0
80	30	0	0	0	0	0	0	0	0.19%

show low error rate, and insensitivity to parameter setting and noise.

Validation of seed detections with real data

Although synthetic data validate algorithms and their implementation, they are no substitute for real data. Our computational method has already been validated for spot detection for 2D cell culture models (Raman *et al.*, 2007). Because foci are counted in 2D through maximum intensity projection within each segmented nucleus, no addition validation is needed. Therefore, with focus on the quality of seed detection in 3D for nuclear segmentation, which has been tested on a data set of 144 colonies, with an average of 20 cells per colony. Each image has $500 \times 500 \times 35$ pixels, and the resolutions along the x, y and z directions are 0.15, 0.15 and 0.75 μm, respectively. Voting parameters for nuclear seed estimation are set as follows: $r_{min} = 1$, $r_{max=60}$, $\Delta_{max} = 20$ and $\Gamma_g = 50$. With the exception of Radon transform (implemented in Matlab and then compiled to C), the entire system is implemented in C++, and the average processing time for one colony data is 12 min on a Linux platform with a 3. GHz CPU, where each colony consists of two stacks of data corresponding to (i) a nuclear channel and (ii) phosphorylation of the DNA repair protein γH2AX. A sample result is shown in Fig. 12.

In this data set, nuclear seeds were first estimated through iterative radial voting, however, approximately 4% of total nuclei did not register correct seeds (error occur in approximately 33% of total colonies), which indicates a detection error rate of 4%. This is presumably due to the abnormal scale and shape of the nuclear volume, and the exact conditions of the nuclei are: (1) *Low contrast between overlapping nuclei:* An absence of gradient information between overlapping nuclei, coupled with their accidental morphological properties, provides ambiguous voting evidence that produces one fixed point instead of two. (2) *Morphological abnormality:* Often, a single nucleus has an abnormal elongated shape, and radial voting merges multiple seed points into a single fixed point. This condition is highly correlated with the previous case. (3) *Incomplete information:* This is due to an imaging problem, where imaging is incomplete and part of the nucleus is missing from the volumetric image, as shown in Fig. 6. (4) *Low sampling resolution in z axis:* The current interpolation algorithm is linear for making a volumetric stack homogeneous in its x, y and the z dimensions. Linear interpolation smoothes the gradient in the z direction, and reduces the contribution of the corresponding gradient information. An improved model will use some form of spline interpolation.

Finally, the error rate for partitioning touching nuclei is approximately 2% (error occur in 9% of total colonies). These errors occur when the optimum plane for separating two nuclei is not the desired plane for partitioning two
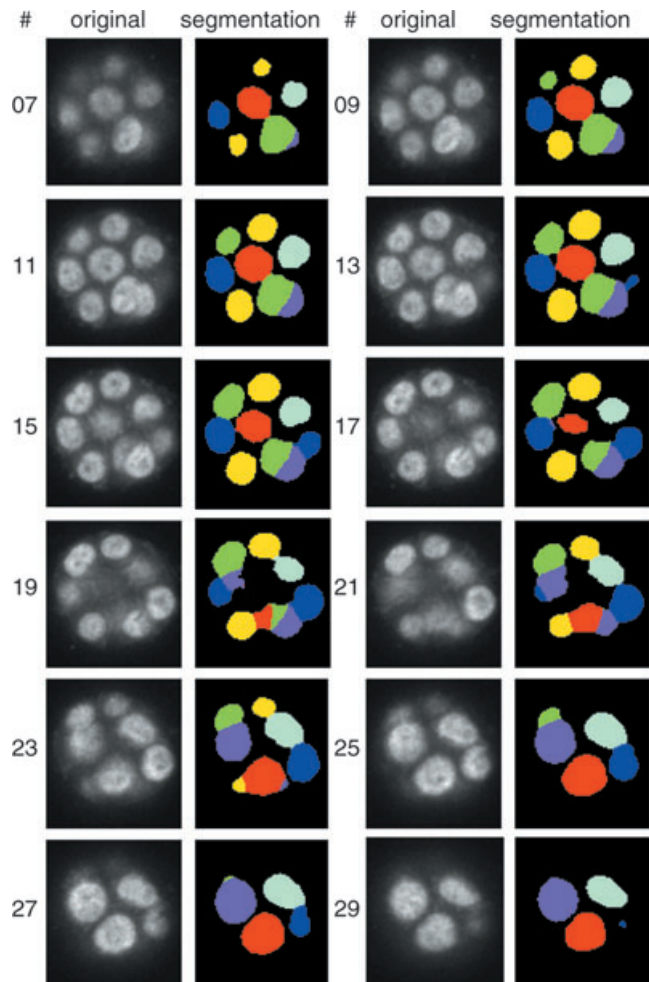

Fig. 12. Segmentation results shown on a subset of slices for an image stack.

neighbouring nuclei. The notion of desired planes has to do with those planes that bisect neighbouring nuclei along points of maximum curvature. In this case, the error rate can be reduced through improved seed estimation.

Case studies for comparison between 2D and 3D cell culture models

We are interested to capture the differences between the 2D and 3D cell culture models at two diverse endpoints under ionizing radiation. Having validated nuclear segmentation, spot counting and building upon on our previous research, we have generated two data sets of phosphorylation histone H2AX (γH2AX) and membrane-bound E-cadherin protein. For both endpoints, we use the same cell line and source of ionizing γ radiation.

(1) In the first experiment, phosphorylation of histone H2AX occurs at sites of DNA double strand breaks (Rogakou *et al.*, 1998) following ionizing radiation. The γ-H2AX foci
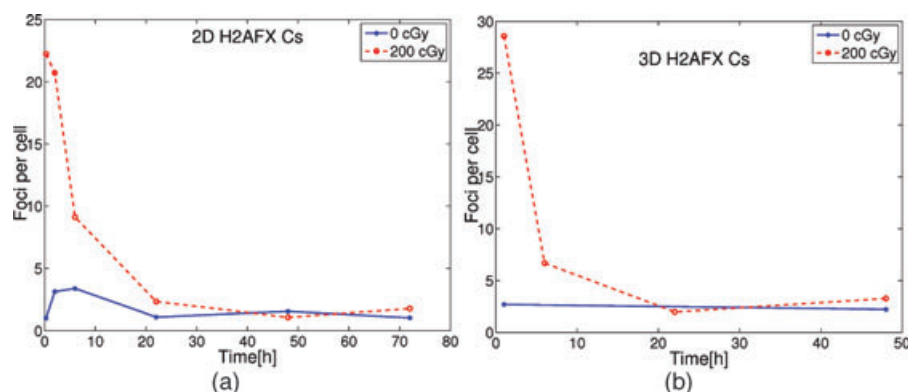
Fig. 13. Kinetics of average number of foci per cell in 2D and 3D cell culture models indicates little difference in the repair efficiency.

formation is considered to be a sensitive biological marker for measuring DNA double strand break induction and repair. We have quantified foci formation at 20 min after exposure to low doses of γ-rays and studied the dephosphorylation of γ-H2AX due to repair of double-strand breaks for up to 72 h in 2D or 48 h in 3D cultures, respectively. We have used our previously published method (Raman *et al.*, 2007) to quantify the γ-H2AX foci formation in 2D cultures. Figure 13 shows preliminary results for noncycling MCF10A cells under different culture conditions (2D or 3D) after exposure to γ-rays. The data shows that the average number of foci per cell, exposed to γ-rays, returns to the background levels within 24 h. In other words, differences between the 2D and 3D culture models are marginal. This result is also in good agreement with pulse field gel electrophoresis (PFGE) data at higher doses (Rydberg *et al.*, 2005).

(2) In the second experiment, involving membrane-bound E-cadherin protein, a total of 118 images were collected for cells grown in 2D and 3D cell culture models and exposed to γ radiation. The data set also includes appropriate control for each assay. We have used our previously published method (Han *et al.*, 2010) to quantify E-cadherin signals for each experiment, and the result is reported in Fig. 14, which indicate that E-cadherin is better preserved in the 3D model systems under identical treatment conditions.

The significance of the earlier two studies is a preliminary result indicating that the endpoints closer to the cell membrane are potentially better preserved in 3D cell culture models as a result of ionizing radiation. Thus, providing further evidence for the utilities of these systems.

Conclusion

This paper presented a series of geometric steps for quantitative analysis of multiple endpoints for 3D cell culture models. The first step estimates an approximation to centre of mass for each nucleus and then partitions a clump of nuclei along minimal intersecting surfaces. Approximate solution to the centre of mass is realized through iterative spatial
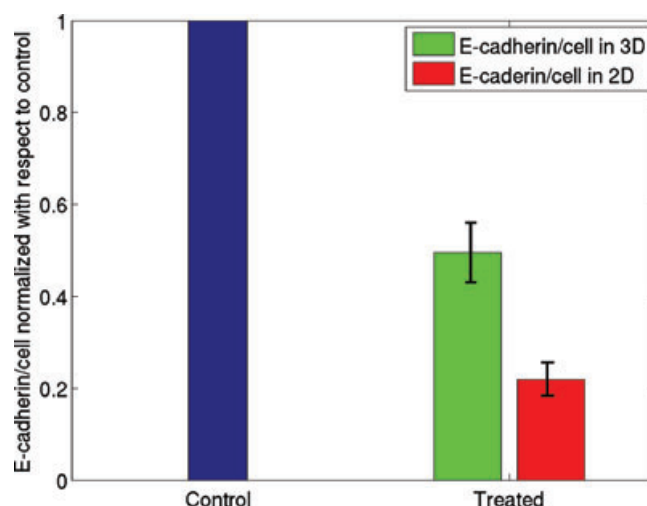

Fig. 14. E-cadherin is better preserved in 3D than in 2D under identical set of treatment.

voting, which is tolerant of variation in shape morphologies, perceptual surfaces, noise and overlapping compartments. These centres of mass are then used to partition a clump of cells along minimal intersecting surfaces that are estimated by Radon transform. The technique has been tested on 144 colonies and their corresponding 3D volumes, and the error rate is fully characterized. Segmentation of the mammosphere provides context for quantifying nuclear-bound macromolecules, where we showed the reuse of iterative voting at a smaller scale. We have applied our computational pipeline to quantify phosphorylation of histone H2AX (γH2AX) in the human breast epithelial cell line MCF10A as a result of ionizing radiation. Comparison between 2D and 3D cell culture models reveal little difference between the two model. This result correlates with the existing literature. However, another endpoint indicated a substantial difference between the two model systems. We hypothesize that these differences are location dependent, and continues to be the subject of our current research.

Acknowledgements

References

Bilmes, J. (1997) A gentle tutorial on the em algorithm and its application to parameter estimation for Gaussian mixture and hidden markov models. *Technical Report ICSI-TR*, 97-021, International Computer Science Institute, Berkeley, CA.

Byun, J., Verardo, M., Sumengen, B., Lewis, G., Manjunath, B. & Fisher, S. (2006) Automated tool for the detection of cell nuclei in digital microscopic images: application to retinal images. *Mol. Vis.* **12**, 949–960.

Carpenter, A., Jones, T., Lamprecht, M., *et al.* (2006) Cellprofiler: image analysis software for identifying and quantifying cell phenotype. *Genome. Biol.* **7**, R100.1–11.

Cavallaro, U. & Christofori, G. (2004) Cell adhesion and signaling: implications for tumor progression. *Nat. Rev. Cancer* **11**, 118–132.

Chan, T. & Vese, L. (2001) Active contours without edges. *IEEE Trans. Image Process.* **10**, 266–277.

Chang, H. & Parvin, B. (2010) Multiphase level set for automated delineation of membrane-bound macromolecules. In *Proceedings of the IEEE International Symposium on Biomedical Imaging*, pp. 165–168. IEEE, Rotterdam, The Netherlands.

Chang, H., Andarawewa, K., Han, J., Barcellos-Hoff, M. & Parvin, B. (2007) Perceptual grouping of membrane signals in cell-based assays. In *Proceedings of the IEEE International Symposium on Biomedical Imaging*, pp. 532–535. IEEE, Washington, DC.

Chawala, M., Lin, G., Olson, K., *et al.* (2004) 3d-catfish: a system for automated quantitative three-dimensional compartmental analysis of temporal gene transcription activity imaged by fluorescence in situ hybridization. *J. Neurosci. Methods.* **139**, 13–24.

Coelho, L.P., Shariff, A. & Murphy, R.F. (2009) Nuclear segmentation in microsope cell images: a hand-segmented dataset and comparison of algorithms. In *Proceedings of the IEEE International Symposium on Biomedical Imaging*, pp. 518–521. IEEE, Boston, MA.

Coelho, L.P., Peng, T. & Murphy, R.F. (2010) Quantifying the distribution of probes between subcellular locations using unsupervised pattern unmixing. *Bioinformatics* **26**, i7–i12.

Deans, S. (1983) *The Radon Transform and Some of Its Applications.* Wiley. Hoboken, NJ.

Duda, R. & Hart, P. (1972) Use of the hough transform to detect lines and curves in pictures. *Comm. ACM* **15**, 11–15.

Han, J., Chang, H., Andarawewa, K., Yaswen, P., Barcellos-Hoff, M. & Parvin, B. (2010) Multidimensional profiling of cell surface proteins and nuclear markers. *IEEE/ACM Trans. Comput. Biol. Bioinform.* **7**, 80–90.

Jackson, C., Murphy, R.F. & Kovacevic, J. (2009) Intelligent acquisition and learning of fluorescence microscope data models. *IEEE Trans. Image Process.* **18**, 2071–2084.

Knowles, D., Sudar, D., Bator-Kelly, C., Bissell, M. & Lelievre, S. (2006) Automated local bright feature image analysis of nuclear protein distribution identifies changes in tissue phenotype. *Proc. Natl. Acad. Sci. USA* **103**, 4445–4450.

Lanzavecchia, S. & Luigi Bellon, P. (1998) Fast computation of 3d radon transform via a direct Fourier method. *Bioinformatics* **12**, 212–216.

Li, G., Liu, T., Tarokh, A., Nie, J., Guo, L., Mara, A., Holley, S. & Wong, S. (2007) 3D cell nuclei segmentation based on gradient flow tracking. *BMC Cell Biol.* **8**(40): 1–10.

Lin, G., Adiga, U., Olson, K., Guzowski, J., Barnes, C. & Roysam, B. (2003) A hybrid 3-d watershed algorithm incorporating gradient cues and object models for automatic segmentation of nuclei in confocal image stacks. *Cytometry* **56A**, 23–36.

Nath, S., Palaniappan, K. & Bunyak, F. (2006) Cell segmentation using coupled level sets and graph-vertex coloring. *Med. Image Comput. Comput. Assist. Interv.* **9**, 101–108.

Otsu, N. (1979) A threshold selection method from gray-level histograms. *IEEE Trans. Sys. Man. Cyber.* **9**, 62–66.

Padfield D., Rittscher J., Thomas N. & Roysam B. (2009) Spatio-temporal cell cycle phase analysis using level sets and fast marching methods. *Med. Image. Anal.* **13**, 143–155.

Parvin, B., Yang, Q., Han, J., Chang, H., Rydberg, B. & Barcellos-Hoff, M.H. (2007) Iterative voting for inference of structural saliency and characterization of subcellular events. *IEEE Trans. Image Process.* **16**, 615–623.

Raman, S., Maxwell, C.A., Barcellos-Hoff, M.H. & Parvin, B. (2007) Geometric approach to segmentation and protein localization in cell culture assays. *J. Microsc.* **225**, 22–30.

Rogakou, E., Pilch, D., Orr, A., Ivanova, V. & Bonner, W. (1998) Dna double-stranded breaks induce histone h2ax phosphorylation on serine 139. *J. Biol. Chem.* **273**, 5858–5868.

Rydberg, B., Cooper, B., Cooper, P., Holley, W. & Chatterjee, A. (2005) Dose-dependent misrejoining of radiation-induced DNA double-strand breaks in human fibroblasts: experimental and theoretical study for high- and low-let radiation. *Radiat. Res.* **163**, 526–534.

Sarti, A., Ortiz De Solorzano, C., Lockett, S. & Malladi, R. (2000) A geometric model for 3-d confocal image analysis. *IEEE Trans. Biomed. Eng.* **47**, 1600–1610.

Srinivasa, G., Fickus, M.C., Guo, Y., Linstedt, A.D. & Kovacevic, J. (2009) Active mask segmentation of fluorescence microscope images. *IEEE Trans. Image Process.* **18**, 1817–1829.

Stuurman, N., Meijne, A.M., van der Pol, A.J., de Jong, L., van Driel, R. & van Renswoude, J. (1990) The nuclear matrix from cells of different origin. Evidence for a common set of matrix proteins. *J. Biol. Chem.* **265**, 5460–5465.

Vese, L. & Chan, T. (2002) A multiphase level set framework for image segmentation using the mumford and shah model. *Int. J. Comput. Vision* **50**, 271–293.

Weaver, V., Fischer, A., Petersen, O. & Bissel, M. (1996) The importance of the microenvironment in breast cancer progression: recapitulation of mammary tumorigenesis using a unique human mammary epithelial cell model and a three-dimensional culture assay. *Biochem. Cell Biol.* **74**, 833–51.

Wen, Q., Chang, H. & Parvin, B. (2009) A Delaunay triangulation approach for segmenting clumps of nuclei. In *Proceedings of the IEEE International Symposium on Biomedical Imaging*, pp. 9–12, IEEE, Boston, MA.

Yang, Q. & Parvin, B. (2003) Harmonic cut and regularized centroid transform for localization of subcellular structures. *IEEE Trans. Biomed. Eng.* **50**, 469–476.

Yin Z., Zhou X., Sun Y. & Wong S.T. (2009) Online phenotype discovery based on minimum classification error model. *Pattern Recognit.* **42**, 509–522.